6th AIAA Atmospheric and Space Environments Conference

16-20 June 2014, Atlanta, Georgia

Aircraft Icing Session

Ice Particle Impacts on a Moving Wedge

Mario Vargas, Peter M. Struk, Richard E. Kreeger
National Aeronautics and Space Administration
Glenn Research Center

José Palacios,
Pennsylvania State University

Kaushik A. Iyer, Robert E. Gold
John Hopkins University Applied Physics Laboratory

This work presents the results of an experimental study of ice particle impacts on a moving wedge. The experiment was conducted in the Adverse Environment Rotor Test Stand (AERTS) facility located at Penn State University. The wedge was placed at the tip of a rotating blade. Ice particles shot from a pressure gun intercepted the moving wedge and impacted it at a location along its circular path. The upward velocity of the ice particles varied from 7 to 12 meters per second. Wedge velocities were varied from 0 to 120 meters per second. Wedge angles tested were 0^0, 30^0, 45^0, and 60^0. High speed imaging combined with backlighting captured the impact allowing observation of the effect of velocity and wedge angle on the impact and the post-impact fragment behavior. It was found that the pressure gun and the rotating wedge could be synchronized to consistently obtain ice particle impacts on the target wedge. It was observed that the number of fragments increase with the normal component of the impact velocity. Particle fragments ejected immediately after impact showed velocities higher than the impact velocity. The results followed the major qualitative features observed by other researchers for hailstone impacts, even though the reduced scale size of the particles used in the present experiment as compared to hailstones was 4:1.

Nomenclature

φ	=	Time delay between the triggering of the pressure gun and the appearance of the frozen droplets at the desired height
τ	=	Time delay between a triggering signal and the appearance of the rotor tip in the field of view
α	=	Wedge angle
AERTS	=	Adverse Environment Rotor Test Stand
APL	=	John Hopkins University Applied Physics Laboratory
D	=	Droplet diameter
FAA	=	Federal Aviation Administration
L	=	Distance from outer face of ice particle to wedge surface
n-p	=	Frame of reference along the surface of the wedge, used for velocity calculations.
s	=	Distance from (x_c, y_c) to the point of impact
t	=	Time it takes the particle starting at (x_f,y_f) to impact the wedge
u	=	Horizontal velocity of the ice particle with respect to the *x-y* frame of reference
v	=	Vertical velocity of the ice particle with respect to the *x-y* frame of reference
V_n	=	Velocity of the ice particle normal to the wedge surface

V_p = Velocity of the ice particle parallel to the wedge surface
W_{wedge} = Wedge velocity
x-y = Frame of reference used to define point locations in the images. Its origin is always located at the upper left corner of the cropped image frame used for data analysis
(x_1, y_1) = Point on the surface of the wedge used together with (x_2, y_2) to obtain the equation of the straight line along the wedge surface
(x_2, y_2) = Point on the surface of the wedge used together with (x_1, y_1) to obtain the equation of the straight line along the wedge surface
(x_c, y_c) = Common point between wedge surface and perpendicular straight line through (x_f,y_f)
(x_d, y_d) = Downward boundary point of the expanding fragment cloud
(x_f, y_f) = Position of the centroid of the ice particle one frame before impact
(x_i, y_i) = Position of the centroid of the ice particle two frames before impact
(x_{impact},y_{impact}) = Impact point of ice particle on wedge surface
(x_u, y_u) = Upward boundary point of the expanding fragment cloud

I. Introduction

Aircraft engine ingestion of ice crystals can cause, at operation conditions, permanent or temporary loss of thrust due to ice accretion accumulation and/or shedding in the engine core[1]. The ice accretion and shedding can affect the performance and/or control of the compressors leading to surging or stalling and in some cases causing permanent damage to the units. It can cause reduction of the clearance between stationary and moving parts affecting their performance. The combustor efficiency and stability may also be affected leading to flame outs. It is a serious in-flight safety problem that has led to new proposed engine certification regulation by the Federal Aviation Administration[2,3].

Since ice accretion on internal engine parts is due to ice crystal impacts, fundamental research efforts have been directed to study the physics involved when ice particles impact on a surface. The studies aim to identify the main parameters involved, the post-impact particle size and velocity distributions, and the main qualitative features of the impact and fragmentation. In these studies the ice crystals are modeled with spherical ice particles. This is needed because complete characterization of the ice particles in a natural environment is not available yet. Also, it is easier to generate spherical particles in a laboratory setting.

Ice crystal impacts are also important in planetary studies. Planning for the collection of ice crystal samples by instrumentation in spacecraft sent to investigate planetary environments requires knowledge of ice crystal impact physics[4]. This interest brought scientists from the John Hopkins University Applied Physics Laboratory to team with NASA and Penn State University researchers who were studying ice crystal impacts on aircraft engines.

Ice particle impacts can be studied in two main configurations: stationary or moving. In a stationary configuration the ice particles are directed towards a stationary target. In a moving configuration the target is moving at a high velocity and impacts an ice particle moving at a lower velocity. This paper presents an investigation of the kinematics of ice particle impacts in a moving configuration. Ice particles shot vertically from a pressure gun impacted a moving wedge placed near the tip of the leading edge of a rotating blade.

The objective of the experiment was to determine if the pressure gun and the rotating wedge could be synchronized to consistently obtain ice particle impacts on the target wedge, capture the event with high speed imaging and observe the effect of velocity and wedge angle on the post-impact fragment behavior. Results were obtained for wedges of 0^0, 30^0, 45^0, and 60^0 moving at velocities from 0 to 120 meters per second. Ice particles were moving at velocities of 7 to 12 meters per second when they were impacted by the wedge. The diameter of the particles varied from 1.5 to 3 millimeters.

In the 1990s, aircraft engine manufacturers dealt with engine ice ingestion problems in the form of hailstones. Excellent studies were conducted at the time by industry and academia on the impact characteristics and numerical models were implemented[5-21]. Because of the differences in size between hailstones and ice crystals, it is not clear if the hailstone results can be directly applied to ice crystal impacts on engine surfaces. But the methodology in those studies can be used as guidance in studying ice crystal impacts. An important objective of ice particle impact studies is to determine if there is a scale effect and whether the main observations from hailstone studies can be maintained or need to be modified. In the present paper the main observations from hailstone results are compared, when possible, to ice particle impact results.

The present work is the first step towards more complete ice particle impact studies in a moving configuration. The results will help determine what additional improvements in the experimental configuration are needed to gain understanding of the kinematics and dynamics of ice crystal impacts on engine components.

II. Method

A. Conceptual View of Experiment

Figure 1 is a conceptual view of the experiment configuration. The particle delivery system (pressure gun) ejects the ice particles towards the expected position of the wedge located near the tip of a blade and rotating with it. At the location where the wedge encounters the ice particle, the light source strikes the mirror mounted near the root of the blade and back-illuminates the impact area. The high speed camera captures the impact. Figure 2 shows the experiment setup. In the sections below each of the setup components is discussed.

B. Ice Particle Preparation

The nominally spherical ice particles (Fig. 3) were prepared using a methodology developed at the John Hopkins University Applied Physics Laboratory. A small quantity of food colorant is dissolved in distilled water. A calibrated pipette is used to allow a distilled water droplet to fall into a Styrofoam cup filled with liquid nitrogen. The colored distilled water droplet freezes on impact and is removed with tweezers to another Styrofoam cup filled with liquid nitrogen where they are collected.

C. Particle Delivery System (Pressure Gun)

To deliver the ice particles, a particle delivery system (pressure gun) was designed and fabricated at the John Hopkins University Applied Physics Laboratory. The pressure gun (Figs. 4 and 5) consists of an inner tube where the ice particles are placed, an outer tube concentric with the inner tube, a tank and a solenoid valve. The space between the two tubes is filled with liquid nitrogen to maintain the temperature of the inner tube at the same temperature as the ice particles and not change their temperature or melt them. The tank is brought to a given target pressure and the solenoid valve is open to eject the ice particles. The tank was pressurized at 33 psi (227 KPa) for all rotor impact tests.

D. Adverse Environment Rotor Test Stand (AERTS), Rotor, Wedge

The Adverse Environment Rotor Test Stand (AERTS) is located at Penn State University[22]. The facility was designed, and is used to test and evaluate rotor blade ice protection systems on full-chord rotor blade sections and under representative centrifugal loads[23]. The AERTS facility is also used for ice protection coating evaluation[24,25] and experimental rotor ice accretion shape correlation to ice shape modeling techniques[26]. The facility is formed by an industrial 6 m x 6 m x 6 m (20 ft x 20 ft x 20 ft) cold chamber where temperatures between -25°C and 0°C (-13°F to 32°F) can be achieved. The chamber is cooled by convection using cooling lines and a set of fans located inside the chamber. The chamber floor is waterproofed with marine lumber covered by aluminum plating and a drainage system along the perimeter of the room which collects melted ice during the post-test defrosting process. Inside the chamber and surrounding the rotor there is a ballistic wall in the shape of an octagon. The ballistic wall is formed by 15.2 cm (6 in) thick weather resistant lumber reinforced with 0.635 cm (0.25 in) thick steel and covered by aluminum plating for weather protection. An 85.5 kilowatt (120 hp) motor rotates the hub and the rotors. Figure 6 shows the chamber and its main components as seen from above.

For the ice particles experiment, the AERTS facility was modified to accommodate high speed visualization of impacts with the rotor tip. Photographs of the hardware arrangement are shown in Fig. 7. To protect the lens of the high speed camera, a 20.3 cm x 20.3 cm x 5 cm (8 in x 8 in x 2 in) ballistic glass was placed on the ballistic wall of the facility. The protective glass was located at the rotor plane level. A diffused light source was placed inside the ballistic wall and under the rotor plane. The light was reflected by a mirror bolted to the rotor grips (Fig. 8). The mirror was positioned such that the light reflection was perpendicular to the plane of the lens when the rotor azimuthal position coincided with the high speed camera position. The mirror adaptor was design to withstand the maximum operational centrifugal loads of the test (1000 g) with a factor of safety of 4. The rotor blades were truncated QH-50 fiber-glass blades. The radius of the rotor was 1.57 m (62 in). The leading edge tip span was 5.08 cm (2 in) and its truncated blades were modified such that wedges could be bolted on at this location. During the experiment, the rotor operated from 0 to 729 rpm (935 g). At the higher rotational speed, the center of the wedge was traveling at 120 m/sec.

At the leading edge tip of the rotor, wedges of 0^0, 30^0, 45^0, and to 60^0 were bolted to the blade using two 4-40 screws. The wedges were made out of aluminum. Span-wise holes on the wedges were made to reduce their weight. Since the light reflecting mirror was offset with respect to the leading edge of the blade, a 2.5 cm (1 in) plastic adapter was also introduced to offset the blade tip wedges (Fig. 9).

E. High Speed Imaging System

High speed imaging was captured using a Vision Research Phantom V611 high-speed digital video camera with a Micro Nikkor 200mm f 4.0 lens. The camera was located behind a piece of 32 mm (1.25 in) ballistic resistant glass (Fig. 10). The camera setup was placed approximately 15.2 cm (6 in) behind the camera window on a large tripod and located in a level orientation. The Phantom camera was operated at maximum resolution of 1280 pixels in the horizontal direction by 800 pixels in the vertical direction. The frames rate used were 6100, 6200 and 22000 frames per second corresponding to time intervals between frames of 163.9, 161.3 and 45.4 μsec. For the slower frame rates, the image resolution of 28 pixels per mm was achieved with the 200 mm lens. For the highest frame rate, only a portion of the imager could be used. To see the entire frame with the highest frame rates, the image resolution was reduced by adding 12 mm of extension tubes (PK-12) which resulted in an image resolution of roughly 11 pixels / mm. The camera exposure time was 1.02 μsec.

The camera system was operated from the control room by means of an Ethernet cable. Files captured to the camera were downloaded over this same Ethernet cable once files were trimmed to the area in the movie where impact occurred. The camera was connected to the triggering mechanisms that allowed for precise timing of capture from each impact event. Trial and error was required to fine tune the timing system. Once the timing was worked out, repeatable triggering was accomplished.

Lighting to the area in which the impacts were going to take place was accomplished with an Arri 575 watt HMI light source and a mirror mounted near the central hub of the blade mechanism. The light was reflected by the mirror for a brief time during the impact event and illuminated the field of view of the camera. The alignment of the light source, mirror and camera was done with a laser pointer. The HMI light source with two layers of diffusion material was placed on the floor of the rotor test facility and a laser pointer was mounted on centerline inside a lens hood attached to the high-speed camera lens. With the laser pointer turned on, the laser beam provided the means to locate the light source in a position that would insure its being seen by the high-speed camera as the rotor blade moved past the camera's position.

III. Synchronization of Test Procedure and Test Matrix

A. Synchronization of Hardware and Imaging System

To ensure impact between the ice particle and the wedge, and to have the camera ready to capture the event, synchronization between the rotor, the pressure gun and the camera must be accomplished. To reach this synchronization, knowing the position of the rotor at a given location along its path (azimuthal position) is required. The rotor azimuthal location was determined using a hall sensor. A magnet was attached to the rotor shaft so that when it traveled in front of the hall sensor (fixed to the bell-housing of the rotor stand), a voltage signal was generated. This signal indicated the azimuthal position of the rotor and triggered the initialization of the video recording capabilities of the camera. The time of travel between the acquisition of the rotor passing signal and the appearance of the rotor tip on the field of view of the high speed camera was the time delay needed for the camera. It was obtained by knowing the recording frames per second of the camera and the number of frames counted from the moment the signal triggered the camera and the appearance of the rotor tip in the field of view. The time delay for the camera was called τ and was measured in milliseconds.

A similar calibration technique was used to determine the time delay of the pressure gun for a given input pressure. This time delay was called the Launch Delay. To calculate the Launch Delay, the time that it took the particles to travel from the triggering of the solenoid valve to the location where the wedge was going to be at impact was needed. This time was called φ and was measured in milliseconds. To calculate φ, a separate trial was done with the camera and the pressure gun. A signal was sent to the solenoid valve controlling the release of pressure inside the pressure gun. The same triggering signal was sent to the initialization of the camera recording capabilities. The time delay, φ, between the triggering of the pressure release valve and the appearance of the frozen drops at the height of the wedge was determined by counting the video frames and knowing the number of frames per second recorded.

Once the time delay between a triggering signal (related to the rotor azimuthal position) and the appearance of the rotor tip on the field of view (called τ), and the time delay between the triggering of the pressure gun and the appearance of the frozen droplets at the desired height location (called φ), the Launch Delay between the triggering signal and the launching of the drops was calculated. The time delay from the rotor triggering signal to the launching of the frozen drops is given by:

$$Launch\ Delay = \tau - \varphi \tag{1}$$

A schematic depicting the time delay of the rotor (top view of the facility) and the time delay of the drop dispenser (side view of the frozen drop dispenser) is shown in Fig. 11. Analog to digital data acquisition software was used to collect 10 data samples of the rotor triggering signal from the Hall sensor at a sampling rate of 20,000 samples/sec. The software also sent signals to a transistor/relay system that triggered the recording capabilities of the camera and the launching of the frozen drops. The time delay between the acquired signal and the output voltage to the transistor/relay system was controllable.

The time delay was a function of the rotor velocity and the pressure of the ice particle dispenser (higher pressures produce higher frozen drop velocities). The calibration process was repeated for each velocity configuration. The pressure of the drop dispenser was maintained constant at 33 psi (227 KPa) for all rotor impact tests.

A final calibration procedure was related to camera height repositioning. The blade grips in the AERTS facility have a 10 degree positive pre-cone angle. The rotor tip positioning decreases in height for higher RPM due to centrifugal loads acting on the blade. The camera height had to be varied accordingly.

B. Test Procedure

Before beginning a run, the high speed camera system was aligned so that the line of sight of the lens was parallel to the direction along the span of the wedge. The camera focus was at the midpoint of the wedge. The alignment of the light source and the mirror was adjusted so that when the wedge was traveling across the camera field of view there was enough illumination for good quality images. The time delays for the camera and the pressure gun were obtained. The space between the inner tube and the outer tube of the pressure gun was filled with liquid nitrogen. The ice particles were prepared and placed in the inner tube of the pressure gun. The tank was set to the target pressure. The time delays for the camera and the pressure gun were input. The rotor was brought to the target velocity and the camera and pressure gun were triggered. The rotor was stopped and the imaging data was examined to determine the quality of the data just obtained. The process was repeated for the next run.

C. Test Matrix

Table I lists the test conditions used in the experiment. A total of 115 runs were completed including runs done to determine the time delays of the pressure gun and the camera. Wedges of four different angles were used: 0^0, 30^0, 45^0 and 60^0. The velocity of the wedge was varied from 0 to 120 meters per second. The main camera frame rates were 6100 and 6200 frames per second. A reduced number of runs were done at camera frame rates of 9528, 13002 and 21003 frames per second.

D. Data Processing

The camera software was used to generate the video clips and to change them from raw format to avi video. The change in format from raw to avi was done without using any compression to avoid altering the data. The camera software was also used to generate a sequence of tiff files for each run. To post process the droplet data from the clips, ImageJ and/or Matlab digital imaging capabilities were used. The programs read the movie in avi format or the tiff files and converted each image frame from grayscale to binary for image segmentation and tracking.

The frame numbers where the tracking begins and ends are selected from the video clip with help of the camera software. The assigned number of the tracked particle is obtained from the frame where the tracking begins. The program identifies the droplets in a given frame by numbering them from left to right. In each frame the digital image processing part of the program calculates and/or records the following parameters for the droplet being tracked: frame number, time with respect to the tracking frame, time with respect to the first frame of the movie, x coordinate of the centroid, y coordinate of the centroid, area, perimeter, major and minor axes of an ellipse superimposed on the droplet, equivalent diameter based on the measured area.

IV. Results and Data Analysis

A. Experimental Configuration to study Ice Particle Impact on a Moving Wedge - Synchronization of Hardware and Imaging System

A main objective of the test was to determine if a rotating wedge and an ice particle shot from a pressure gun could be timed so that an impact on the target could be obtained with some degree of repeatability and captured with high speed imaging. This objective presented three issues: (1) how to make the ice particles; (2) how to shoot them in a consistent and controllable manner; (3) how to time the motion of the wedge, the pressure gun and the high

speed imaging to obtain an impact on the target and to capture it consistently. The fabrication of the particles was accomplished by dropping a water droplet in liquid nitrogen. The shooting of the particles in a controllable manner was accomplished with a pressure gun that was designed to keep the barrel at the same temperature as the ice particles. A methodology was designed to accomplish the timing of the wedge motion, the pressure gun and the high speed camera. The method was successful and the experiment was conducted. Back illumination of the field of view and the ice particles required a series of pre-experiment tests. Those tests allowed to determine the camera and mirror illumination optimal configuration and the camera frame rates needed.

B. Fragment Cloud Edge Velocity

Studies by Guégan et al.[5,6] and Pan and Render[7-13] on the impact of hail-size ice particles showed very high velocities for the first ejected fragments during impact. The velocity of those first ejected fragments was higher than the approaching ice particle velocity before impact. In the present experiment the velocity of the edge of the fragment cloud was measured to determine if at the reduced size of the ice particles tested, the initial ejected fragments exhibited the same behavior.

Figure 12 shows the impact sequence for Run 85 071113. In the image the wedge is moving from left to right. The velocity of the wedge is 120 m/sec, the vertical velocity of the ice particle (upward in the image) is 9 m/sec, the wedge angle is 30^o, the diameter of the ice particle is 2.9 millimeters, the camera frame rate is 6200 frames per second, and the camera resolution is 27.5 pixels per millimeter. In the first frame (frame 46), the wedge is not visible yet. The ice particle that moves upwards can be seen. In the second frame (frame 47) the upper part of the wedge and the ice particle are captured. In the third frame (frame 48) the impact has occurred. The cloud of fragments is visible on the surface of the wedge and extends upwards and downwards over the surface. Because there is a time difference of 161.3 microseconds between each image frame, the actual moment and location of the impact were not captured in the images and need to be calculated to obtain the upward and downward velocity of the fragment cloud.

Figures 13 and 14 illustrate the procedure followed to calculate the upward and downward velocities. Figure 13 shows the geometry of the wedge and the parameters used in the calculations. The input parameters are printed in blue; the calculated parameters are printed in red. The following are the input parameters:

- (x_i,y_i) and (x_f,y_f) are the position of the centroid of the ice particle in the two frames previous to the impact (for example, frames 46 and 47 of Fig. 12). Since the time between frames is known, the x and y velocities of the particle before impact can be calculated.
- (x_1,y_1) and (x_2,y_2) are two points chosen on the surface of the wedge to define the equation of the edge line of the wedge. The points are selected so that (x_1,y_1) is above the impact point and (x_2,y_2) below. These points are measured in the frame previous to the impact (frame 47 of Fig. 12).
- (x_u,y_u) and (x_d,y_d) are the upward and downward boundary points of the expanding fragment cloud. The coordinates for these two points are obtained from the impact frame (frame 48 of Fig. 12) and their values are adjusted to the previous frame where all the calculations are being done. Since the y values are the same in both frames, only the x values need to be adjusted. This is done by subtracting from the x values the distance in pixels that the wedge has moved from one frame to the other: $V_{wedge}\cdot$(1/frame rate)$\cdot$1000$\cdot$resolution.
- The ice particle diameter is measured in the frame prior to impact (frame 47 of Fig. 12).
- The frame rate, the camera resolution and the wedge angle are all parameters fixed during the running of the experiment.

Figure 14 shows the flow diagram for the calculations and the equations used. Two frames of reference were used in the calculations. The *x-y* frame of reference with the origin of coordinates at the upper left corner of the images is used to define point locations. The *n-p* frame of reference with n normal to the wedge and p along the surface of the wedge is used for the velocity calculations. Both frames of reference are shown in green in Fig. 13.

As shown in figure 14 (second box), after the input parameters are obtained, (x_i,y_i) and (x_f,y_f) are used to calculate the horizontal (u) and vertical (v) velocity of the ice particle with respect to the *x-y* frame of reference. Those velocities, together with the velocity and angle of the wedge, are used to calculate the velocity components of the particle with respect to the *n-p* frame of reference. The velocities normal and parallel to the surface of the wedge are labeled V_n and V_p respectively. The next step in the calculation (third box) is to obtain the coordinates of the point (x_c, y_c). This point is located on the surface of the wedge and is also the perpendicular line traced from the centroid of the ice particle (x_f,y_f) to the wedge surface. Knowing the equation of the straight line running along the surface of the wedge and the equation of the straight line perpendicular to it and passing through the known point (x_f, y_f) allows the calculation of the coordinates of the common point (x_c, y_c). Next, the distance between the points (x_f,y_f) and (x_c, y_c) minus the radius of the ice particle is calculated and labeled L. The distance L divided by the

normal velocity V_n gives the time it takes the particle starting at (x_f,y_f) to impact the wedge. This time and the velocity parallel to the wedge surface V_p are used to calculate the distance from the point (x_c, y_c) to the impact point. This distance is labeled *s* in Figs. 13 and 14. The distance s together with the coordinates of the point (x_c, y_c) allows the calculation of the coordinates of the point of impact (x_{imp}, y_{imp}) as shown in the fourth box of Fig. 14. Knowing the coordinates of the point of impact, and (x_u,y_u) and (x_d,y_d), the upward and downward boundary points of the expanding fragment cloud, the distance that the edge of the cloud has moved since the time of impact can be obtained. This distances minus the radius of the ice particle, divided by the time since the impact occurred gives the up and down velocities of the fragment cloud (Fig. 14, fifth box). The radius is subtracted because it is assumed that the leading ejected fragments come from the thickest part of the ice particle.

Figure 15 shows the impact frame for Run 85 071113. The impact point is indicated. The table below the frame shows the coordinates of the impact point, the wedge velocity and the upward and downward velocity of the cloud. Because the cloud extends to the upper and lower points of the frame, the actual extreme boundary of the cloud could be outside the frame. The velocities in this case and in similar cases analyzed should be considered as lower bound velocities.

Table 2 lists the results for all runs of the experiment where the fragment cloud velocity was measured. The parameters measured in the flow chart of Fig. 13 are listed. For Run 85 071113 the upward velocity was measured at 117.8 m/sec. The downward velocity was measured at 240.2 m/sec. At the time of impact the velocity normal to the wedge was -108.8 m/sec and the velocity parallel to the surface of the wedge was -52.4 m/sec. The sign indicates the direction of the velocity with respect to the n-p axis of reference. The overall impact velocity was 120.8 m/sec. The cloud boundary extends to the end of the frame. Both velocities are lower bound estimates. The velocity of the fragment cloud is higher than the incoming velocity of the particle.

Pan and Render[7-13] observed that the velocity of the fragment cloud decreases rapidly as the cloud expands. This indicates that the higher fragment cloud velocities should occur right after the time of impact. In Run 96 071213 a particle was captured right after impact and the cloud velocities measured. Figure 16 shows the impact sequence. Figure 17 shows the impact frame with the impact point and the upward and downward limits of the cloud. The table below the frame in Fig. 17 contains the velocity of the wedge and the upward and downward fragment cloud velocity. The additional parameters calculated or measured are listed in Table 2 under Run 96 071213. The upward and downward velocities were 326.3 and 388.1 m/sec respectively. At impact, the particle had a velocity of -120.2 m/sec normal to the wedge and a velocity of 10.3 m/sec parallel to the wedge surface. The sign indicates the direction of the velocity with respect to the n-p reference system. The particle impacted at a total velocity of 120.6 m/sec. The upward and downward velocities were three times larger than the ice particle impact velocity.

All the measured cloud fragment velocities are listed in Table 2 and confirm observations by Guégan et al. and Pan and Render that the initial ejected fragments after impact have higher velocities than the velocity of the impacting particle. In cases where the velocity of the cloud edge was lower it was due to the fact that the cloud edge extended beyond the image frame and the value obtained was a lower bound value. The measurements indicate that at the reduced size scale the fragment cloud shows the same velocity behavior as observed for the larger hailstones. The large velocity of the small fragments can be explained as follows: at the initial point of impact small fragments form that receive the high kinetic energy carried by the ice particle. Because of their small size, the kinetic energy received manifests itself in very high velocities.

C. Additional General Observations

Although the quantitative measurements are limited by the side view of the impact, the side view configuration allows additional qualitative general observations on fragment size and how far the fragments rebound after impact.

Fragment size was found to decrease with the impact kinetic energy. This can be expected because the higher the impact energy, the more fracture cracks are created in the particle.

One of the important observations of Guégan et al. and Pan and Render when studying impact of hailstones was the very shallow angle at which the particle fragments move in a direction perpendicular to the impact surface[5,6,17]. Angles of less than 2^o were observed. Particle fragments bounce very little; they spread over the surface. These observations refer to particles impacting at high velocities. To verify this with the smaller size ice particles used in the present experiment, the distance of fragment rebound was measured normal to the wedge surface in the first post-impact image. At the lower velocities the fragments can rebound a large distance from the wedge surface. As the velocity is increased, the rebound distance decreases and at 120 m/sec it was measured to be less than 6 millimeters. This agrees with what was observed by Guégan et al. and Pan and Render.

V. Conclusions

In the experiment conducted at the Adverse Environment Rotor Test Stand (AERTS) facility, ice particles shot from a pressure gun impacted on a moving wedge at a location along its circular path. The upward velocity of the ice particles varied from 7 to 12 meters per second. Wedge velocities were varied from 0 to 120 meters per second. Wedge angles tested were 0^0, 30^0, 45^0, and 60^0. High speed imaging combined with backlighting captured the impact and allowed to observe the effect of velocity and wedge angle on the impact and the post-impact fragment behavior. From the analysis of the data the following conclusions can be stated:

- A rotating wedge and an ice particle shot from a pressure gun can be timed so that an impact on the target can be obtained with some degree of repeatability and captured with high speed imaging. The experimental configuration allows the study of ice particle impacts on a moving surface.

- The data showed that the velocities of the first ejected fragments that formed the edge of the cloud were higher than the approaching ice particle velocity before impact. This result agrees with work done by researchers studying the impact of hailstones on flat plate targets. At the reduced size scale of the ice particles tested compared to the hailstones in the studies, the ejected fragments at the edge of the fragment cloud exhibited the same behavior as observed for hailstones.

- At the higher velocity tested, 120 meters per second, the fragments after impact tended to have a low bounce normal to the wedge, compared to the motion of the fragments along the surface of the wedge. This also agrees with previous observations from studies on hailstone impacts on a flat surface.

The results of the work presented here will help in the design of future experiments of ice particle impacts on a moving surface. The experiments are needed to understand the physics involved in the impact of ice crystals on moving elements in turbofan engines which is one of the current main areas of engine icing studies. Future experiments on the impact characteristics of ice crystals on engine spinner, fan and core components in terms of post-impact particle size distribution, particle velocity distribution and direction of travel, and effect of partial melting of crystals will provide experimental data to develop and validate numerical models.

Acknowledgments

The authors would like to thank Mr. Chris Lynch for his excellent imaging work during the experiment. Mr. Hadi Navid and Mr. Andrew Webb, both with JHU/APL, led the design, fabrication and proofing of the ice particle dispenser. The present work is part of the NASA collaboration under a Space Act Agreement. It is funded by the Atmospheric Environment Safety Technologies (AEST) Project, Aviation Safety Program (AvSP). Special thanks to Dr. Ron Colantonio for his support of the effort.

References

[1]Mason, J. G., Strapp, J.W., and Chow, P., "The Ice Particle Threat to Engines in Flight," *AIAA 2006-206*, 44th AIAA Aerospace Sciences Meeting and Exhibit, Reno NV, January 2006

[2]Electronic Code of Federal Regulations, Title 14, Part 33, "Airworthiness Standards: Aircraft Engines," *[Online]*, http://www.ecfr.gov/cgi-bin/text-idx?c=ecfr&tpl=/ecfrbrowse/Title14/14tab_02.tpl [Cited March 12, 2014].

[3]Federal Register Proposed Rules, Airplane and Engine Certification Requirements: "Supercooled Large Drop, Mixed Phase, and Ice Crystal Icing Conditions," *FR DOC #: 2010-15726*, Vol. 75, No. 124, pp. 37311-37339, June 29, 2010.

[4]Wall, M., "Saturn Moon Enceladus Eyed for Sample-Return Mission" SPACE.com, December 2012, http://www.space.com/18792-enceladus-sample-return-mission.html

[5]Guégan, P., Othman, R., Lebreton, D., Pasco, F., Villedieu, P., Meyssonnier, J., and Wintenberger, S., "Experimental Investigation of the Kinematics of Post-impact Ice Fragments," *International Journal of Impact Engineering*, Vol. 38, No. 10, 2011, pp. 786-795.

[6]Guégan, P., Othman, R., Lebreton, D., Pasco, F., Villedieu, P., Meyssonnier, J., and Wintenberger, S., "Critical impact velocity for ice fragmentation," *Proc IMechE Part C, J Mechanical Engineering Science*, Vol. 226, No. 7, 2011, pp. 1677-1682.

[7]Render, P.M., Pan, H., Sherwood, M., Riley, S.J., "Studies into the hail ingestion characteristics of turbofan engines," *AIAA 93-2174*, AIAA/SAE/ASME/ASEE 29th Joint Propulsion Conference, Monterey CA, June 1993.

[8]Pan, H., Render, P.M., "Experimental studies into the hail ingestion characteristics of turbofan engines," *AIAA 94-2956*, AIAA/SAE/ASME/ASEE 30th Joint Propulsion Conference, Indianapolis, IN, June 1994.

[9]Render, P.M., Pan, H., "Experimental studies into hail impact characteristics," *J Propulsion and Power*, Vol. 11, No. 6, 1995, pp. 1224-1230.

[10]Pan, H., Render, P.M., "The influence of target rotation on impact characteristics of simulated hailstones," *AIAA 95-3038*, AIAA/SAE/ASME/ASEE 31ts Joint Propulsion Conference, San Diego, CA, June 1995.

[11]Pan, H., Render, P.M., "Impact characteristics of hailstones simulating ingestion by turbofan aeroengines," *J Propulsion and Power*, Vol. 12, No. 3, 1996, pp. 457-462.

[12]Pan, H., Render, P.M., "Effects of target curvature on the impact characteristics of simulated hailstones," *Proceedings of the Institution of Mechanical Engineers, Part G: Journal of Aerospace Engineering*, Vol. 211, No. 2, 1997, pp. 81-90.

[13]Pan, H., Render, P.M., "Studies into hail ingestion of turbine engines using a rotating fan and spinner assembly" *Aeronautical Journal*, Vol. 102, 1998, pp. 45-51.

[14]Rosin, P., Rammler, E., "The laws governing the fitness of powdered coal", *J Inst Fuel*, Vol. 7, 1933, pp. 29-36.

[15]Tuhkuri, J., "Analysis of ice fragmentation process from measured particle size distribution of crushed ice," *Cold Regions Science and Technology*, Vol. 23, No. 1, 1994, pp. 69-82.

[16]Hamdi E., du Mouza J., "A methodology for rock mass calibration and classification to improve blast results," Int J Rock Mech Min Sci, Vol. 42, 2005, pp. 177-194.

[17]AGARD Report AR-332, September 1995

[18]Araoka, K., and Maeno, N., "Measurements of restitution coefficients of ice" *Low Temp. Sci., Ser. A*, Vol. 36, 1978, pp. 55-65 [in Japanese with English summary].

[19]Hatzes, A.P., Bridges, F. G., and Lin, D.N.C., "Collisional properties of ice spheres at low impact velocities." *Monthly Notices of the Royal Astronomical Society*, Vol. 231, 1988, pp. 1091-1115.

[20]Higa, M., Arakawa, M., and Maeno, N., "Measurements of restitution coefficients of ice at low temperatures", *Planetary and Space Science*, Vol. 44, No. 9, 1996, pp. 917-925.

[21]Higa M., Arakawa, M., Maeno, N., "Size dependence of restitution coefficients of ice in relation to collision strength" *Icarus*, Vol. 133, No. 2, 1998, pp. 310-320.

[22]Palacios, J., Han, Y., Brouwers, E., Smith, E., "Icing Environment Rotor Test Stand Liquid Water Content Measurement Procedures and Ice Shape Correlation," *American Helicopter Society Journal*, Vol. 57, No. 2, 2012, paper number 022006.

[23]Overmeyer, F.A., Palacios, J., and Smith, E., "Ultrasonic De-Icing Bondline Design and Rotor Ice Testing", *AIAA Journal*, Vol. 51, No. 12, 2013, pp. 2965-2976.

[24]Brouwers, E., Peterson, A., Palacios, J., Centolanza, L., "Ice Adhesion Strength Measurements for Rotor Blade Edge Materials," *67th Annual Forum Proceedings - American Helicopter Society*, Virginia Beach, VA, May, 2011.

[25]Soltis, J., Palacios, J., Wolfe, D., Eden, T., "Evaluation of Ice Adhesion Strength on Erosion Resistant Materials," *AIAA-2013-1509*, 54th AIAA/ASME/ASCE/AHS/ASC Structures, Structural Dynamics, and Materials Conference, 2013, Boston, Massachusetts, April 2013.

[26]Han, Y., Palacios, J., Schmitz, S., "Scaled Ice Accretion Experiments on a Rotating Wind Turbine," *Journal of Wind Engineering and Industrial Aerodynamics*, Vol. 109, July 2012, pp. 55-67.

Table 1. Test Matrix

Run	Date	Lens	Aperture	Frame Rate	Spatial Resolution	Ice Gun Pressure	Wedge Angle	Rotor Speed	Rotor Velocity at Impact
-	-	-	-	fps	pix / mm	psia	degrees	RPM	m/s
1	7/8/2013	200 mm only	4.0	6200	28.6	30	0	232.0	38.3
2	7/8/2013	200 mm only	4.0	6200	28.6	30	0	232.0	38.3
3	7/8/2013	200 mm only	4.0	6200	28.6	30	0	0.0	0.0
4	7/8/2013	200 mm only	4.0	6200	28.6	50	0	0.0	0.0
5	7/9/2013	200 mm only	4.0	6200	28.6	N/A	45	242.6	40.0
6	7/9/2013	200 mm only	4.0	6200	28.6	50	45	243.0	40.1
7	7/9/2013	200 mm only	4.0	6200	28.6	50	45	243.0	40.1
8	7/9/2013	200 mm only	4.0	6273	28.6	50	45	242.9	40.1
9	7/9/2013	200 mm only	4.0	6200	28.6	50	45	242.7	40.0
10	7/9/2013	200 mm only	4.0	6200	28.6	50	N/A	0.0	0.0
11	7/9/2013	200 mm only	4.0	6200	28.6	50	45	243.5	40.2
12	7/9/2013	200 mm only	4.0	6200	28.6	50	45	243.4	40.1
13	7/9/2013	200 mm only	4.0	6200	28.6	50	60	243.3	40.1
14	7/9/2013	200 mm only	4.0	6200	28.6	50	60	243.4	40.1
15	7/9/2013	200 mm only	4.0	6200	28.6	50	30	243.0	40.1
16	7/9/2013	200 mm only	4.0	6200	28.6	50	30	243.0	40.1
17	7/9/2013	200 mm only	4.0	6200	28.6	50	30	243.0	40.1
18	7/9/2013	200 mm only	4.0	6200	28.6	50	N/A	0.0	0.0
19	7/9/2013	200 mm only	4.0	6200	28.6	50	N/A	0.0	0.0
20	7/9/2013	200 mm only	4.0	6200	28.6	33	N/A	0.0	0.0
21	7/9/2013	200 mm only	4.0	6200	28.6	33	30	243.1	40.1
22	7/9/2013	200 mm only	4.0	6200	28.6	33	30	243.1	40.1
23	7/9/2013	200 mm only	4.0	6200	28.6	33	0	243.1	40.1
24	7/9/2013	200 mm only	4.0	6200	28.6	33	0	243.1	40.1
25	7/9/2013	200 mm only	4.0	6200	28.6	33	0	243.1	40.1
26	7/9/2013	200 mm only	4.0	6200	28.6	N/A	0	486.2	80.2
27	7/9/2013	200 mm only	4.0	6200	28.6	33	0	486.2	80.2
28	7/9/2013	200 mm only	4.0	6200	28.6	33	0	485.7	80.1
29	7/9/2013	200 mm only	4.0	6200	28.6	33	0	485.5	80.1
30	7/9/2013	200 mm only	4.0	6200	28.6	33	0	485.6	80.1
31	7/9/2013	200 mm only	4.0	6200	28.6	33	30	485.7	80.1
32	7/10/2013	105 mm + PK12	2.8	22003	11.2	N/A	30	485.5	80.1
33	7/10/2013	105 mm + PK12	2.8	22003	11.2	N/A	30	485.5	80.1
34	7/10/2013	105 mm + PK12	2.8	22003	11.2	33	N/A	0.0	0.0
35	7/10/2013	105 mm + PK12	2.8	22003	11.2	33	30	485.5	80.1
36	7/10/2013	105 mm + PK12	2.8	22003	11.2	33	30	485.6	80.1
37	7/10/2013	105 mm + PK12	2.8	22003	11.2	33	30	485.6	80.1
38	7/10/2013	105 mm + PK12	2.8	22003	11.2	33	30	485.8	80.1
39	7/10/2013	105 mm + PK12	2.8	22003	11.2	33	30	485.7	80.1
40	7/10/2013	200	4.0	6200	27.7	N/A	30	486.0	80.1
41	7/10/2013	200	4.0	6200	27.7	33	N/A	0.0	0.0
42	7/10/2013	200	4.0	6200	27.7	33	30	486.0	80.1
43	7/10/2013	200	4.0	6200	27.7	33	30	485.6	80.1
44	7/10/2013	200	4.0	6200	27.7	33	N/A	0.0	0.0
45	7/10/2013	200	4.0	6200	27.7	33	30	485.8	80.1
46	7/10/2013	200	4.0	6200	27.7	33	30	485.6	80.1
47	7/10/2013	200	4.0	6200	27.7	33	30	485.6	80.1
48	7/10/2013	200	4.0	6200	27.7	33	45	486.2	80.2
49	7/10/2013	200	4.0	6200	27.7	33	45	485.5	80.1
50	7/10/2013	200	4.0	6200	27.7	33	45	485.5	80.1
51	7/10/2013	200	4.0	6200	27.7	33	60	486.0	80.1
52	7/10/2013	200	4.0	6200	27.7	33	60	485.4	80.0
53	7/10/2013	200	4.0	6200	27.7	33	60	486.0	80.1
54	7/10/2013	200	4.0	6200	27.7	N/A	60	486.0	80.1
55	7/10/2013	200	4.0	6200	27.7	33	60	486.0	80.1
56	7/10/2013	200	4.0	6200	27.7	33	60	486.0	80.1
57	7/10/2013	200	4.0	6200	27.7	N/A	60	728.4	120.1
58	7/10/2013	200	4.0	6200	27.7	33	60	728.0	120.1

Table 1. Test Matrix (Continuation)

Run	Date	Lens	Aperture	Frame Rate	Spatial Resolution	Ice Gun Pressure	Wedge Angle	Rotor Speed	Rotor Velocity at Impact
59	7/10/2013	200	4.0	6200	27.7	N/A	60	728.6	120.2
60	7/10/2013	200	4.0	6200	27.7	33	60	728.7	120.2
61	7/10/2013	200	4.0	6200	27.7	33	60	728.4	120.1
62	7/10/2013	200	4.0	6200	27.7	53	60	0.0	0.0
63	7/10/2013	200	4.0	6200	27.7	43	60	0.0	0.0
64	7/10/2013	200	4.0	6200	27.7	38	60	0.0	0.0
65	7/10/2013	200	4.0	6200	27.7	33	60	0.0	0.0
66	7/10/2013	200	4.0	6200	27.7	27	60	0.0	0.0
67	7/10/2013	200	4.0	6200	27.7	22	60	0.0	0.0
68	7/11/2013	200	4.0	6200	27.5	17	60	0.0	0.0
69	7/11/2013	200	4.0	6200	27.5	17	60	0.0	0.0
70	7/11/2013	200	4.0	6200	27.5	17	60	0.0	0.0
71	7/11/2013	200	4.0	6200	27.5	17	60	0.0	0.0
72	7/11/2013	200	4.0	6200	27.5	15	60	0.0	0.0
73	7/11/2013	200	4.0	6200	27.5	15	60	0.0	0.0
74	7/11/2013	200	4.0	6200	27.5	15	60	0.0	0.0
75	7/11/2013	200	4.0	6200	27.5	15	60	0.0	0.0
76	7/11/2013	200	4.0	6200	27.5	15	60	0.0	0.0
77	7/11/2013	200	4.0	6200	27.5	33	45	728.7	120.2
78	7/11/2013	200	4.0	6200	27.5	33	45	0.0	0.0
79	7/11/2013	200	4.0	6200	27.5	33	45	728.9	120.2
80	7/11/2013	200	4.0	6200	27.5	33	45	729.0	120.2
81	7/11/2013	200	4.0	13002	27.5	33	45	729.1	120.2
82	7/11/2013	200	4.0	9528	27.5	33	30	729.0	120.2
83	7/11/2013	200	4.0	6200	27.5	33	30	728.8	120.2
84	7/11/2013	200	4.0	6200	27.5	33	30	729.5	120.3
85	7/11/2013	200	4.0	6200	27.5	33	30	729.8	120.4
86	7/11/2013	200	4.0	6200	27.5	33	0	728.8	120.2
87	7/11/2013	200	4.0	6200	27.5	33	0	728.8	120.2
88	7/11/2013	200	4.0	6200	27.5	33	0	728.8	120.2
89	7/11/2013	200	4.0	6100	27.5	33	0	728.8	120.2
90	7/11/2013	200	4.0	6100	27.5	33	0	0.0	0.0
91	7/11/2013	200	4.0	6100	27.5	33	0	0.0	0.0
92	7/11/2013	200	4.0	6100	27.5	33	0	728.7	120.2
93	7/12/2013	200	4.0	6100	27.5	33	0	728.7	120.2
94	7/12/2013	200	4.0	6100	27.5	33	0	728.8	120.2
95	7/12/2013	200	4.0	6100	27.5	33	0	728.8	120.2
96	7/12/2013	200	4.0	6100	27.5	33	0	728.8	120.2
97	7/12/2013	200	4.0	6100	27.5	33	0	728.8	120.2
98	7/12/2013	200	4.0	6100	27.5	33	0	486.0	80.1
99	7/12/2013	200	4.0	6100	27.5	33	0	485.5	80.1
100	7/12/2013	200	4.0	6100	27.5	33	0	486.0	80.1
101	7/12/2013	200	4.0	6100	27.5	33	0	488.0	80.5
102	7/12/2013	200	4.0	6100	27.5	33	0	243.0	40.1
103	7/12/2013	200	4.0	6100	27.5	33	0	242.8	40.0
104	7/12/2013	200	4.0	6100	27.5	33	0	242.8	40.0
105	7/12/2013	200	4.0	6100	27.5	33	0	242.8	40.0
106	7/12/2013	200	4.0	6100	27.5	33	0	120.6	19.9
107	7/12/2013	200	4.0	6100	27.5	33	0	122.5	20.2
108	7/12/2013	200	4.0	6100	27.5	33	0	122.5	20.2
109	7/12/2013	200	4.0	6100	27.5	33	0	122.5	20.2
110	7/12/2013	200	4.0	6100	27.5	33	0	122.5	20.2
111	7/12/2013	200	4.0	6100	27.5	33	0	91.5	15.1
112	7/12/2013	200	4.0	6100	27.5	33	0	91.5	15.1
113	7/12/2013	200	4.0	6100	27.5	33	0	91.5	15.1
114	7/12/2013	200	4.0	6100	27.5	33	0	91.5	15.1
115	7/12/2013	200	4.0	6100	27.5	33	0	91.5	15.1

Table 2. Fragment Cloud Velocity

Run Number	frame_i	frame_f	frame_impact	xu	yu	xd	yd	x1	y1	x2	y2	xi	yi	xf	yf	Diameter	Diameter	WedgeAngle	resolution
Dimensionless				Pixels	Pixels	Pixels	Pixels	Pixels	pixels	pixels	pixels	Pixels	Pixels	Pixels	Pixels	Pixels	mm	Degrees	Pixels/mm
070913_Run11	11	12	13	162	335	-144	659	533	-40	174	788	312	427	315	361	88	3.1	45	27.9
070913_Run14	15	16	17	152	161	78	206	290	83	-181	466	312	427	315	361	96	3.4	60	28.6
070913_Run23	35	36	37	296	37	315	633	295	81	296	800	360	430	363	373	82	2.9	0	28.6
070913_Run25	44	45	46	39	8	36	290	40	62	40	781	193	355	193	300	88	3.1	0	28.6
071013_Run43	11	12	13	602	397	485	587	769	138	393	800	630	514	655	488	18	0.7	30	27.6
071213_Run_85	46	47	48	229	1	-191	799	159	124	34	350	347	336	347	296	79	2.9	30	27.5
071213_Run_87	50	51	52	360	0	360	800	360	58	360	196	422	296	426	257	77	2.8	0	27.5
071113_Run_88	46	47	48	217	42	217	800	217	121	217	584	429	646	435	604	37	1.3	0	27.5
071113_Run_89	54	55	56	102	1	102	442	102	25	102	385	485	220	489	183	77	2.8	0	27.5
071213_Run_95	44	45	46	-83	1	-83	754	-83	25	-83	625	146	112	148	67	52	1.9	0	27.5
071213_Run_96	44	45	46	-430	545	-430	683	-430	555	-430	665	121	709	121	663	48	1.7	0	27.5
071113_Run_100	43	44	45	41	115	41	561	41	135	41	475	295	405	298	369	41	1.5	0	27.5
071113_Run_101 -26	24	25	26	-151	135	-151	270	-151	150	-151	250	197	283	199	244	40	1.5	0	27.5
071113_Run_101-403	401	402	403	44	1	44	541	44	125	44	325	226	240	227	216	75	2.7	0	27.5
071113_Run_104	14	15	16	253	1	253	303	253	25	253	225	311	201	314	161	47	1.7	0	27.5
071113_Run_105	30	31	32	2	286	2	800	2	375	2	675	78	645	78	606	54	2.0	0	27.5
071213_Run_113	28	29	30	1	201	1	478	1	255	1	395	42	392	41	352	48	1.8	0	27.5

Table 2. Fragment Cloud Velocity (continuation)

Run Number	xc	yc	L	u	v	Vn	Vp	t	s	ximpact	yimpact	Cloud Velocity Down	Cloud Velocity Up	Wedge Velocity
Dimensionless	Pixels	Pixels	Pixels	m/sec	m/sec	m/sec	m/sec	seconds	meters	Pixels	Pixels	m/sec	m/sec	m/sec
070913_Run11	50	444	28	-0.7	-13.5	-39.2	-20.2	2.552E-05	5.153E-04	40	454	-73	45	45
070913_Run14	207	131	142	0.8	-14.4	-31.8	-26.2	1.561E-04	4.089E-03	106	190	-211	368	368
070913_Run23	296	311	29	0.8	-12.4	-39.5	12.4	2.567E-05	3.177E-04	296	302	-85	68	68
070913_Run25	39	210	102	0.0	-12.0	-40.4	12.0	8.817E-05	1.058E-03	39	180	-53	82	82
071013_Run43	579	382	76	5.7	-5.5	-67.2	-32.4	4.104E-05	1.331E-03	561	414	-58	12	12
071213_Run_85	132	172	208	0.0	-9.0	-108.8	-52.4	6.968E-05	-3.650E-03	82	259	-240	118	120
071213_Run_87	360	257	28	0.9	-8.8	-119.3	8.8	8.428E-06	7.411E-05	360	255	-130	61	120
071113_Run_88	217	604	199	1.3	-9.6	-118.9	9.6	6.098E-05	5.837E-04	217	588	-77	198	120
071113_Run_89	102	183	348	0.7	-8.3	-119.5	8.3	1.059E-04	8.740E-04	102	159	-177	99	120
071213_Run_95	-83	67	205	0.4	-10.0	-119.8	10.0	6.210E-05	6.212E-04	-83	50	-251	17	120
071213_Run_96	-430	663	527	-0.1	-10.3	-120.3	10.3	1.593E-04	1.640E-03	-430	618	-326	388	120
071113_Run_100	41	369	237	0.8	-8.0	-79.3	8.0	1.087E-04	8.725E-04	41	345	-129	138	80
071113_Run_101 -26	-151	244	330	0.3	-8.6	-80.2	8.6	1.495E-04	1.290E-03	-151	209	-103	135	81
071113_Run_101-403	44	216	146	0.3	-5.5	-80.2	5.5	6.623E-05	3.643E-04	44	205	-111	62	81
071113_Run_104	253	161	38	0.8	-8.9	-39.2	8.9	3.509E-05	3.121E-04	253	152	-36	36	40
071113_Run_105	2	606	49	0.0	-8.5	-40.0	8.5	4.448E-05	3.798E-04	2	596	-54	86	40
071213_Run_113	1	352	16	-0.2	-8.8	-15.3	8.8	3.721E-05	3.268E-04	1	343	-32	34	15

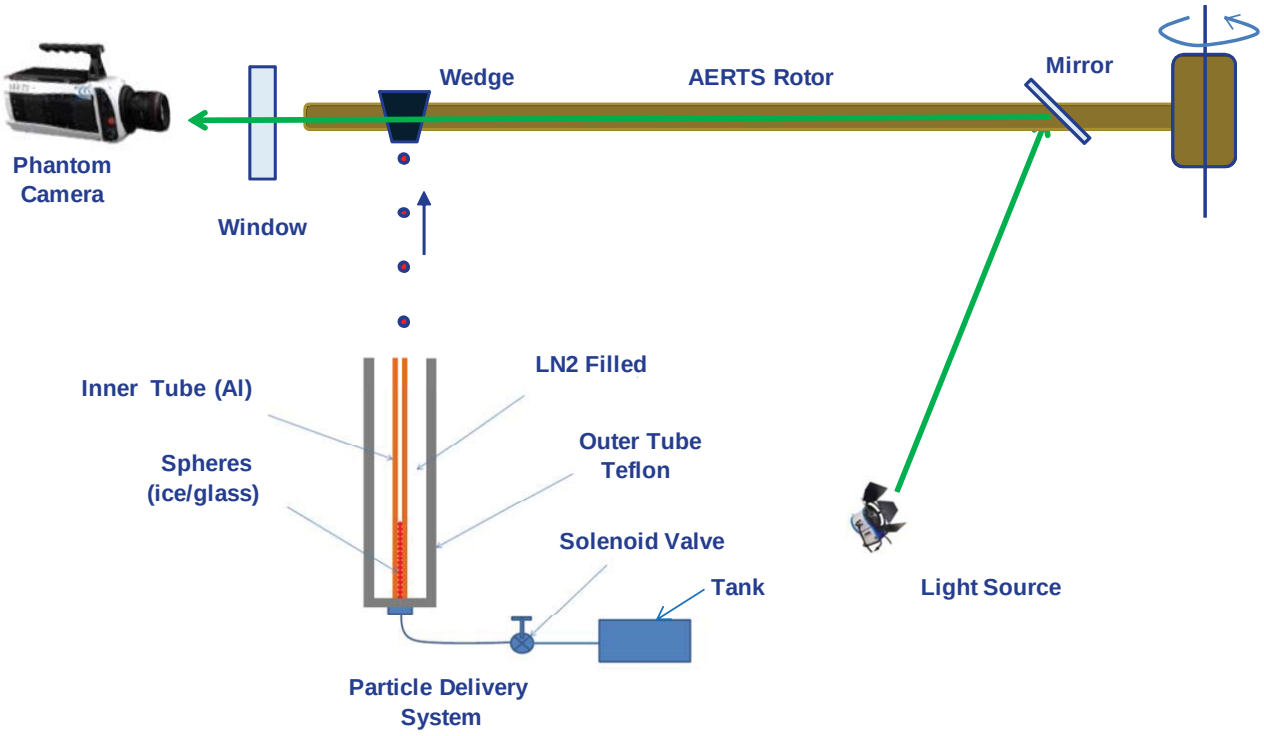

Figure 1. Conceptual View of the Experiment

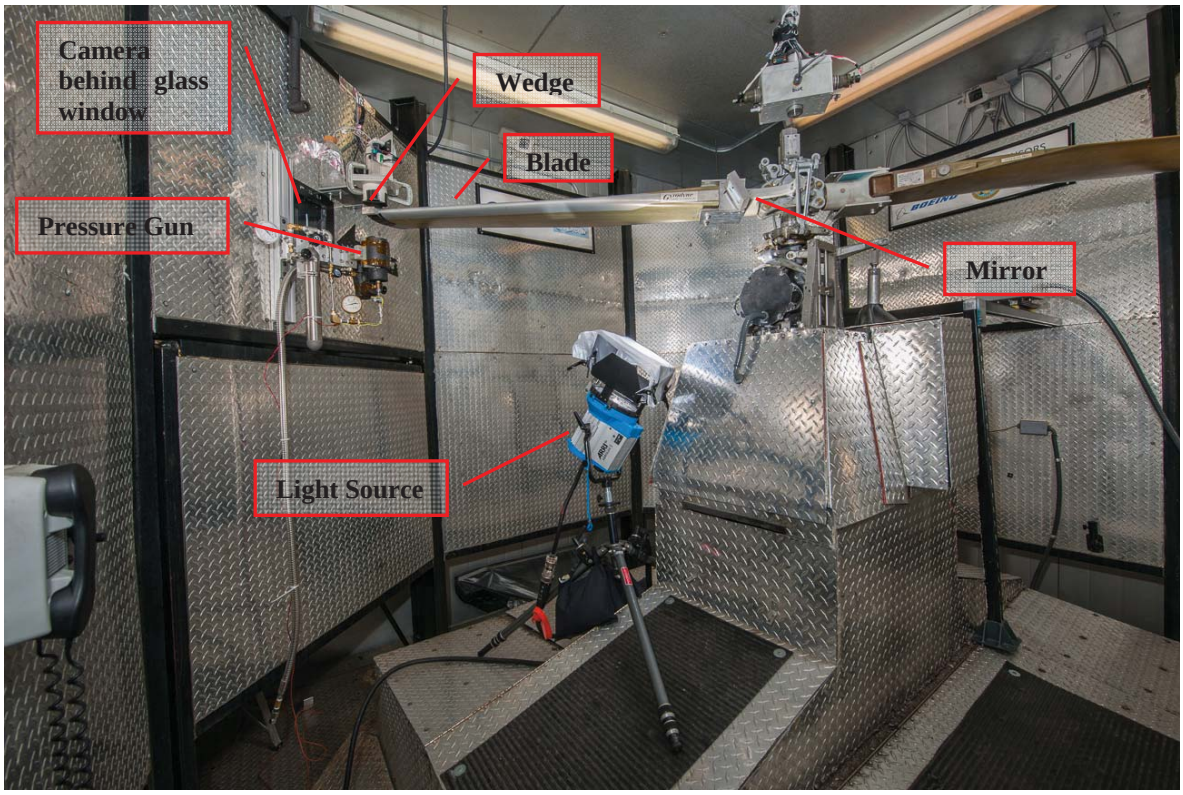

Figure 2. Experiment Setup

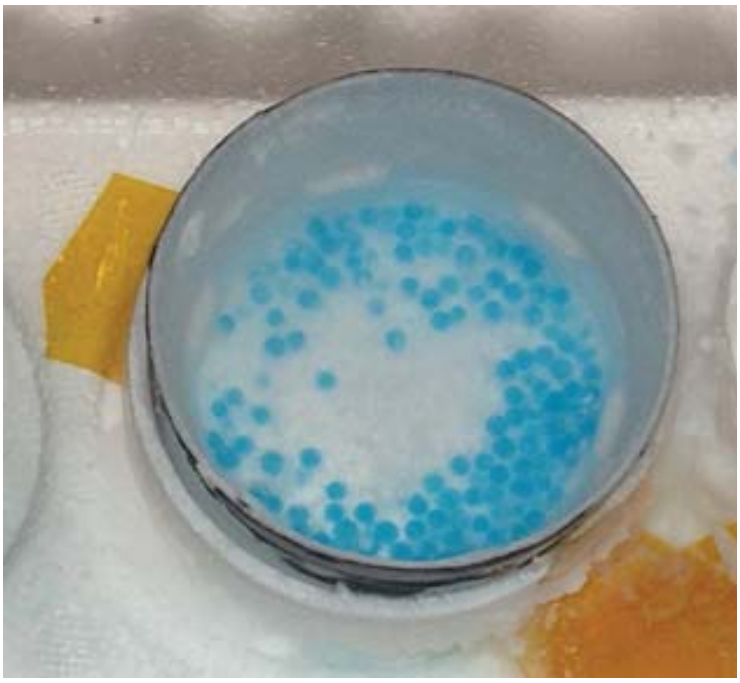

Figure 3. Ice Particles

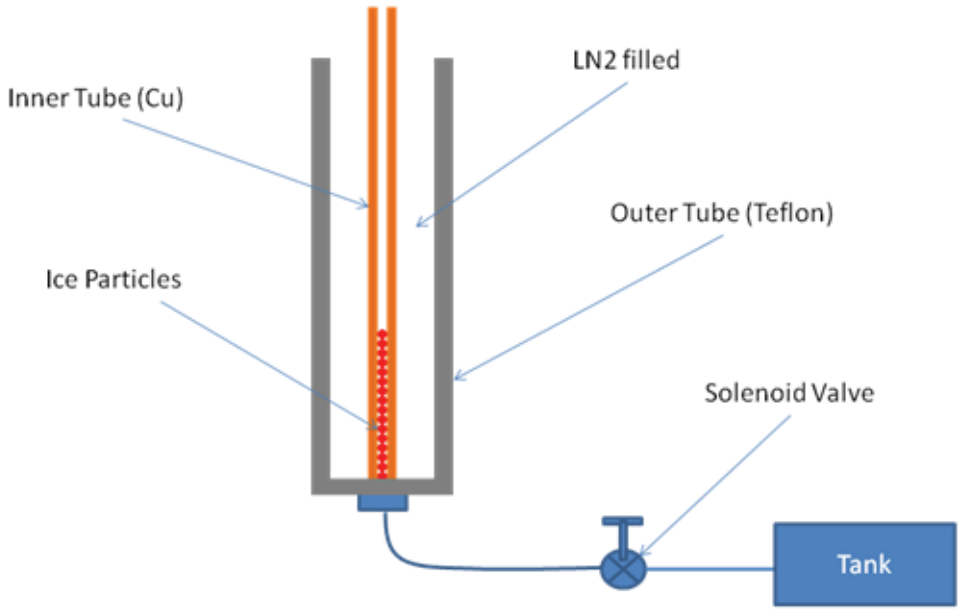

Figure 4. Schematic of Particle Delivery System (Pressure Gun). The main components are shown: inner tube, outer tube, pressure tank and solenoid valve

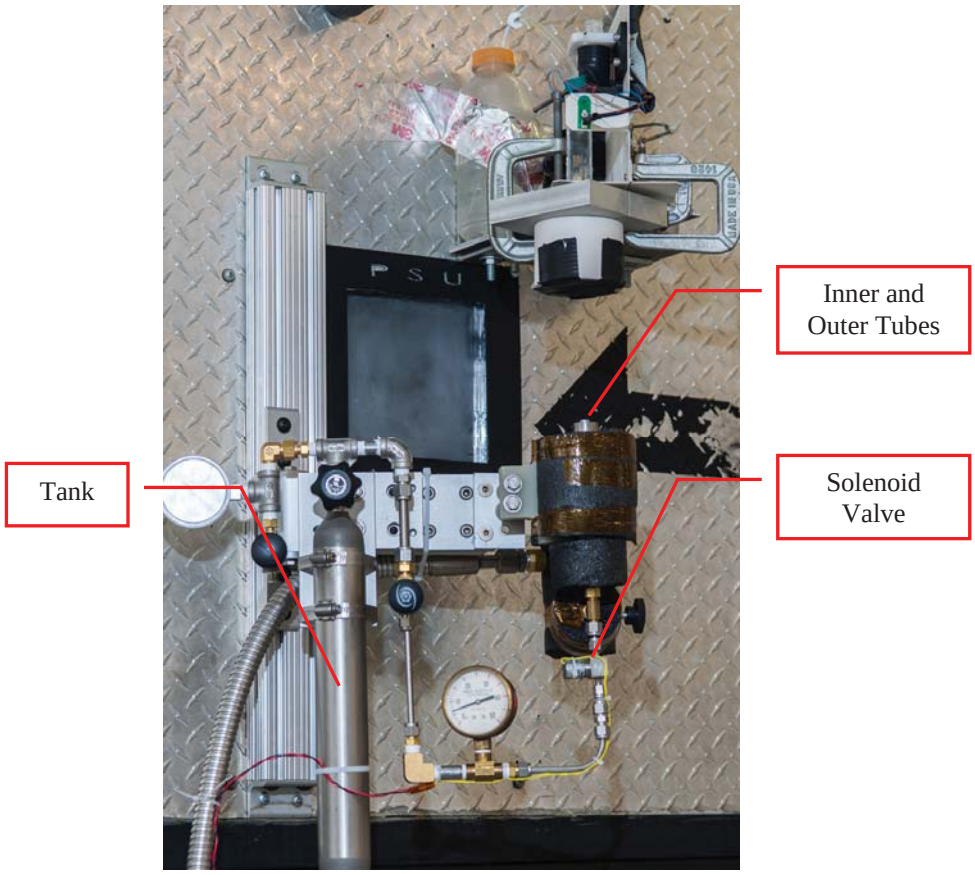

Figure 5. Particle Delivery System (Pressure Gun). Dark area below the inner and outer tube label is insulation material surrounding the two tubes.

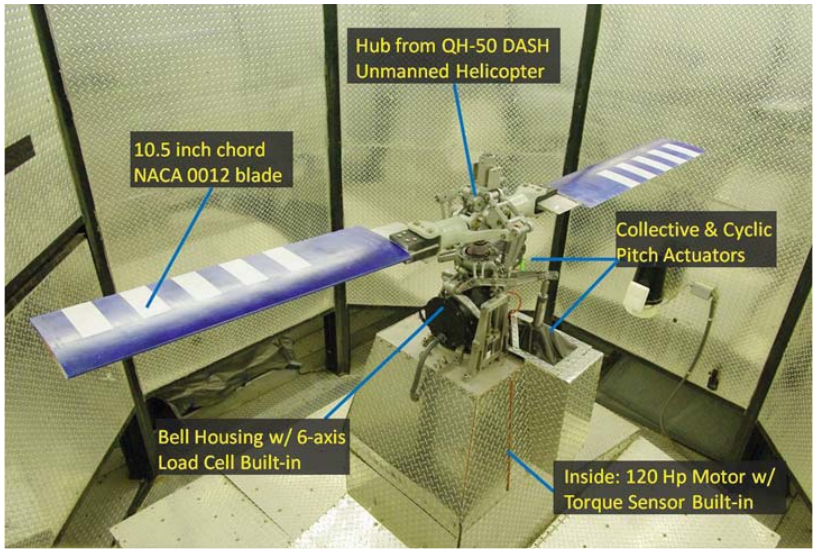

Figure 6. Adverse Environment Rotor Test Stand (AERTS) facility at Penn State University

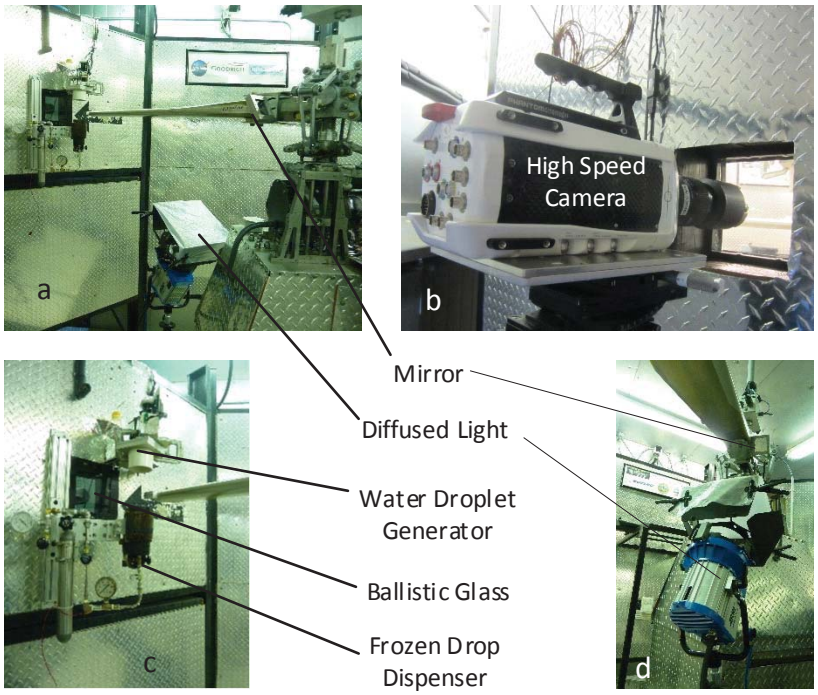

Figure 7. Hardware installation: a) Rotor blade view from blade root to tip, b) Detail of blade tip region, c) Detail of blade root region, d) Detail of high speed camera behind ballistic wall

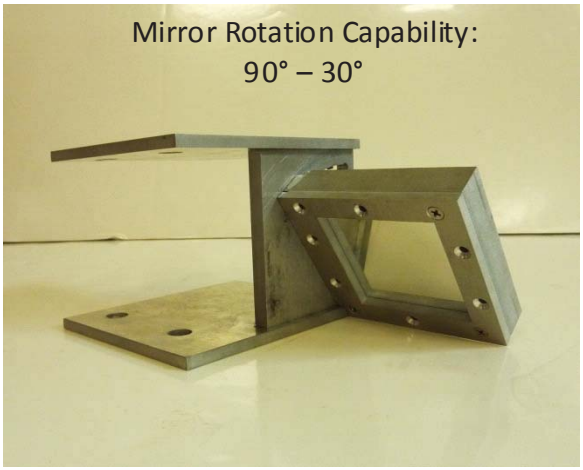

Figure 8. Photograph of adjustable mirror located at the blade root

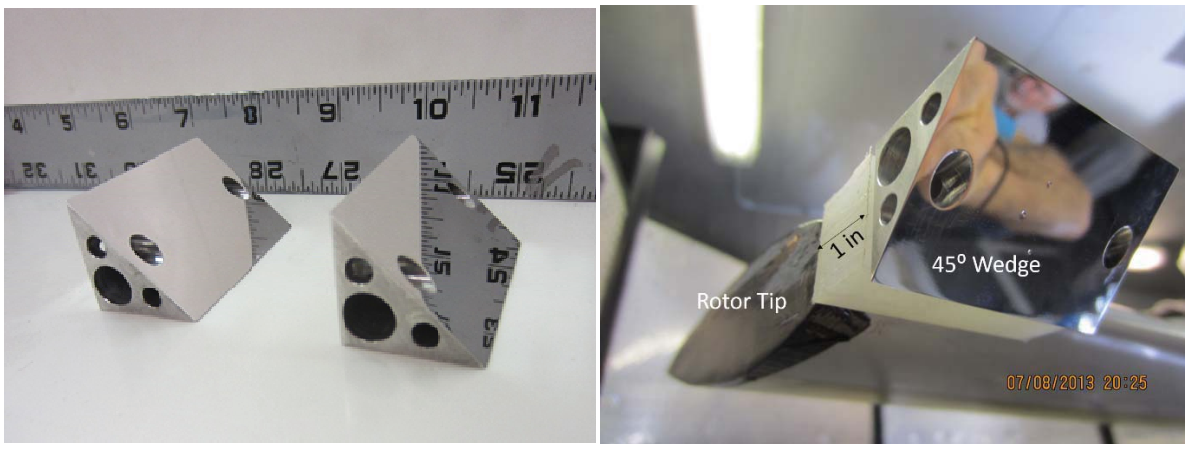

Figure 9. Photograph of 45^0 wedges and detail of installation on rotor tip.

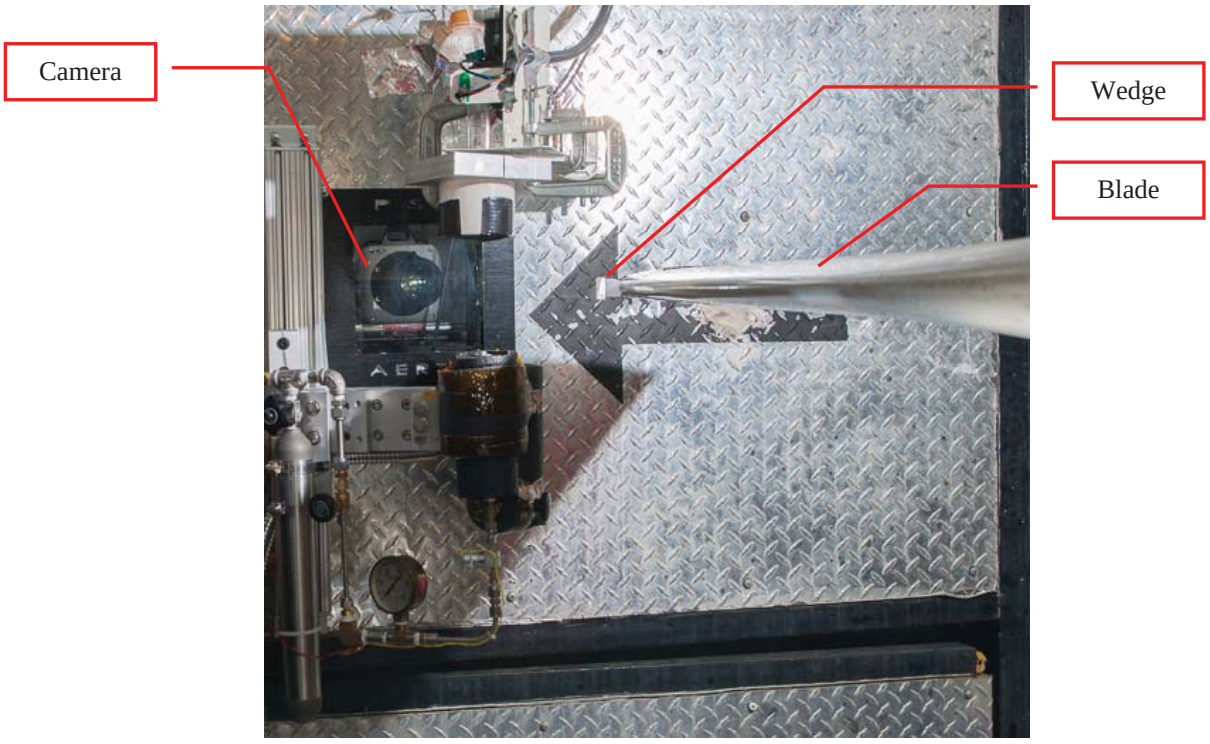

Figure 10. Camera behind glass window. Wedge and blade are also indicated.

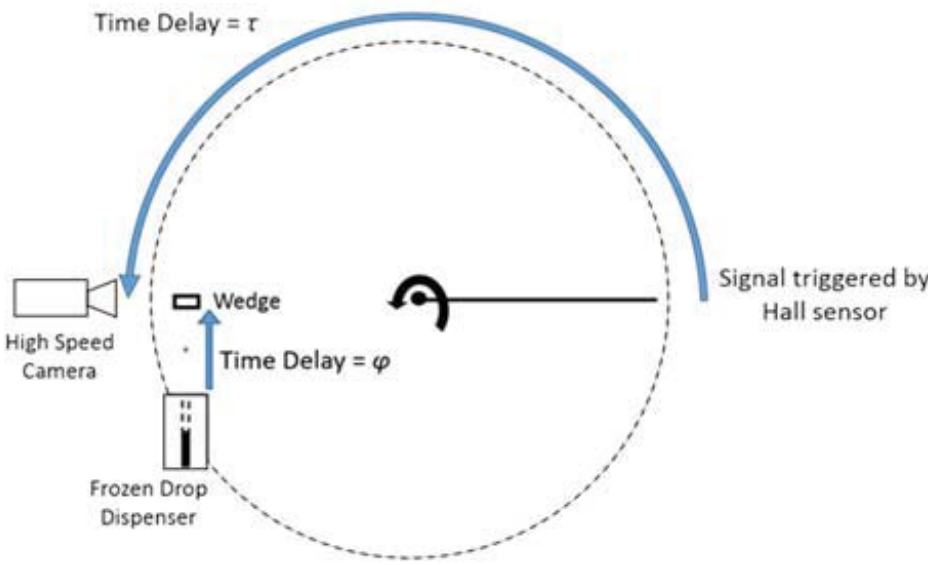

Figure 11. Schematic time delay calculation to determine frozen drop launch from rotor passing triggering signal.

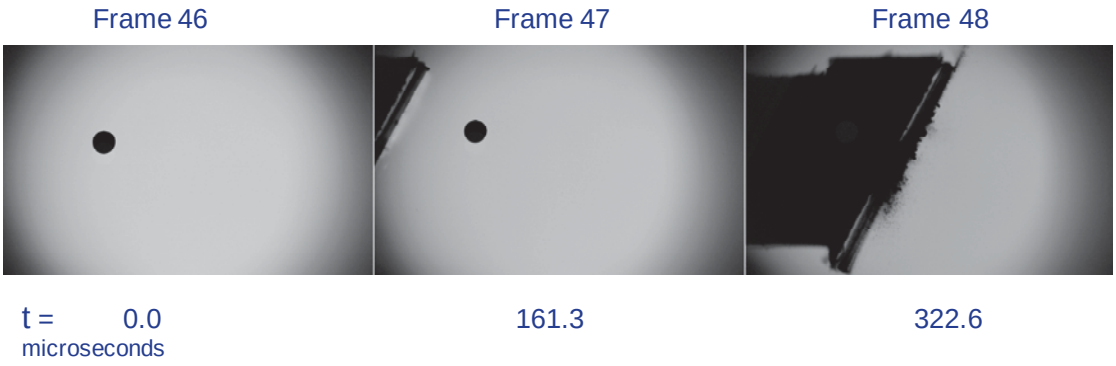

Figure 12. Impact sequence for Run 85 071113. Wedge moving from left to right. V_{wedge} = 120 m/sec; vertical velocity of ice particle $V_{particle}$ = 9 m/sec; wedge angle 30°, ice particle diameter = 2.9 millimeters; camera frame rate = 6200 fps; camera resolution = 27.5 pixels/millimeter. The particle was calculated to impact the wedge at t = 231.0 microseconds, a time occurring between frame 47 and 48.

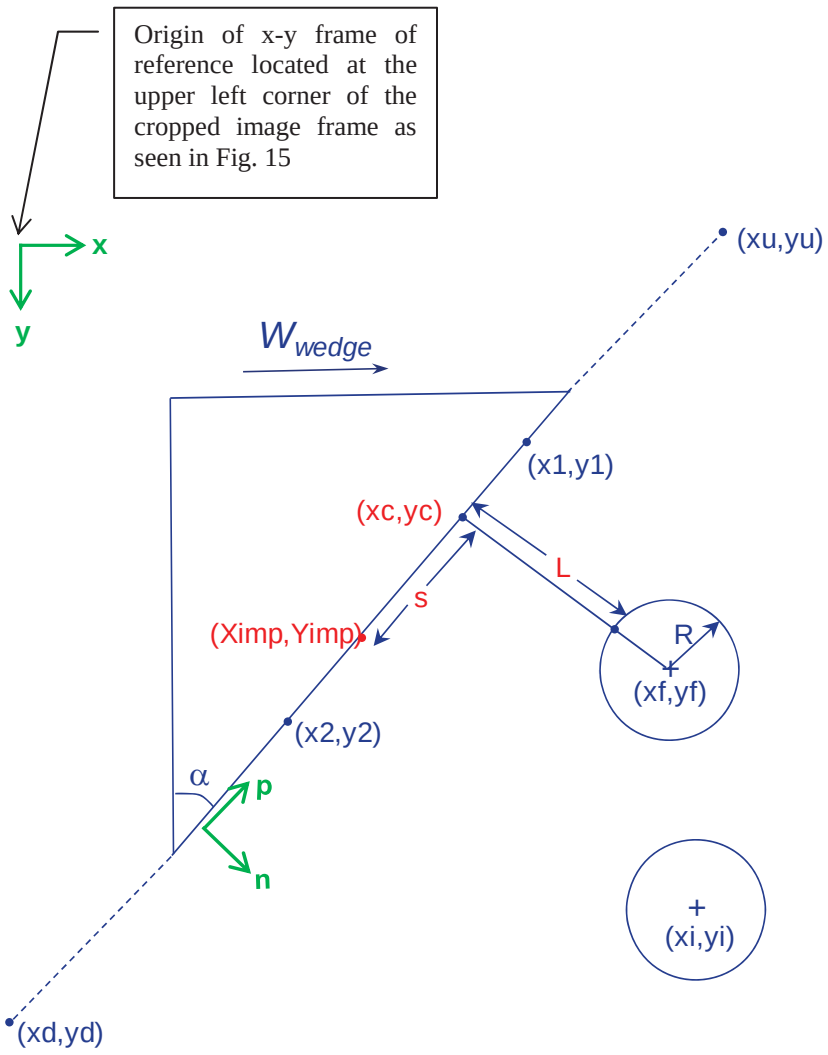

Figure 13. Drawing of wedge and parameters used to calculate the velocity of the fragment cloud. Input parameters are in blue, calculated parameters in red, and frames of reference in green.

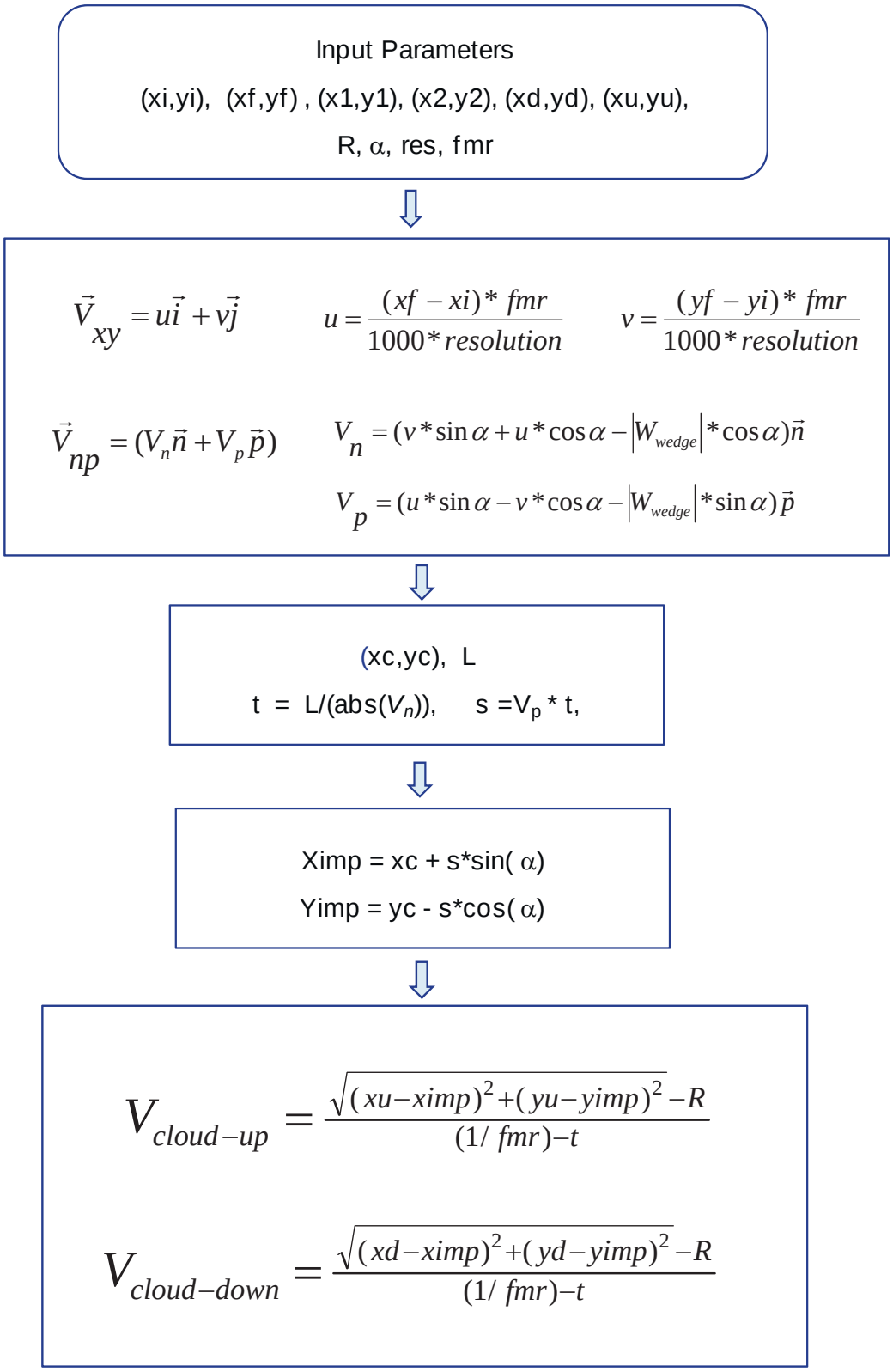

Figure 14. Flowchart showing the input parameters and the equations used in the calculation of the upward and downward velocities of the fragment cloud.

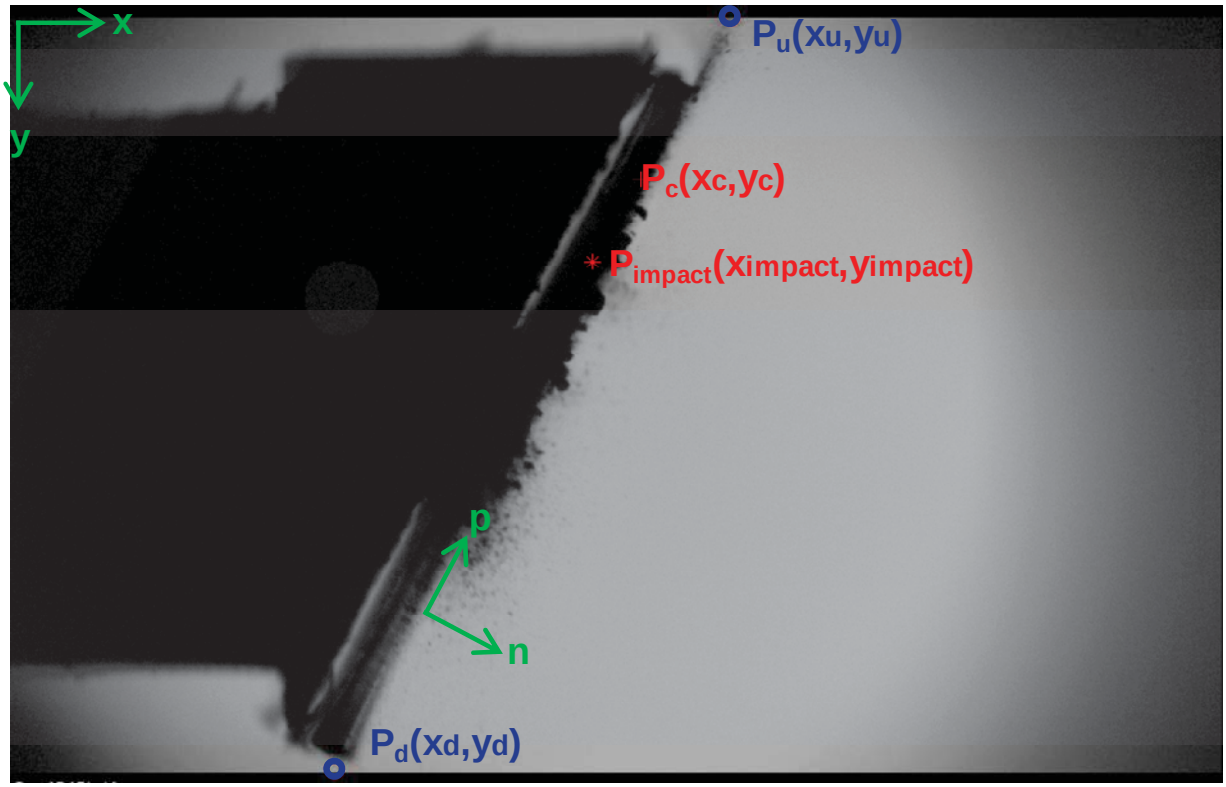

ximpact	yimpact	Cloud Velocity Down	Cloud Velocity Up	Wedge Velocity
Pixels	Pixels	m/sec	m/sec	m/sec
82.2	259.0	-240.2	117.8	120.4

Figure 15. Run 85 071113. Input parameters are in blue, calculated parameters in red, and frames of reference in green. The impact point is shown. V_{wedge} = 120 m/sec; $V_{particle}$ = 9 m/sec; wedge angle 30°, ice particle diameter = 2.9 millimeters; camera frame rate = 6200 fps; camera resolution = 27.5 pixels/millimeter.

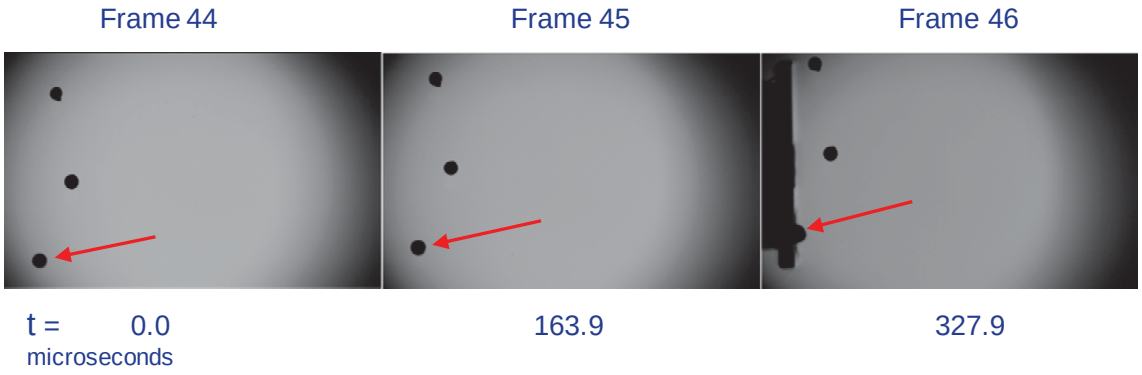

Figure 16. Impact sequence for Run 96 071213. Wedge moving from left to right. V_{wedge} = 120.2 m/sec; vertical velocity of ice particle $V_{particle}$ = 10.3 m/sec; wedge angle 0°, ice particle diameter = 1.7 millimeters; camera frame rate = 6100 fps; resolution = 27.5 pixels/millimeter. Particle studied is indicated with a red arrow.

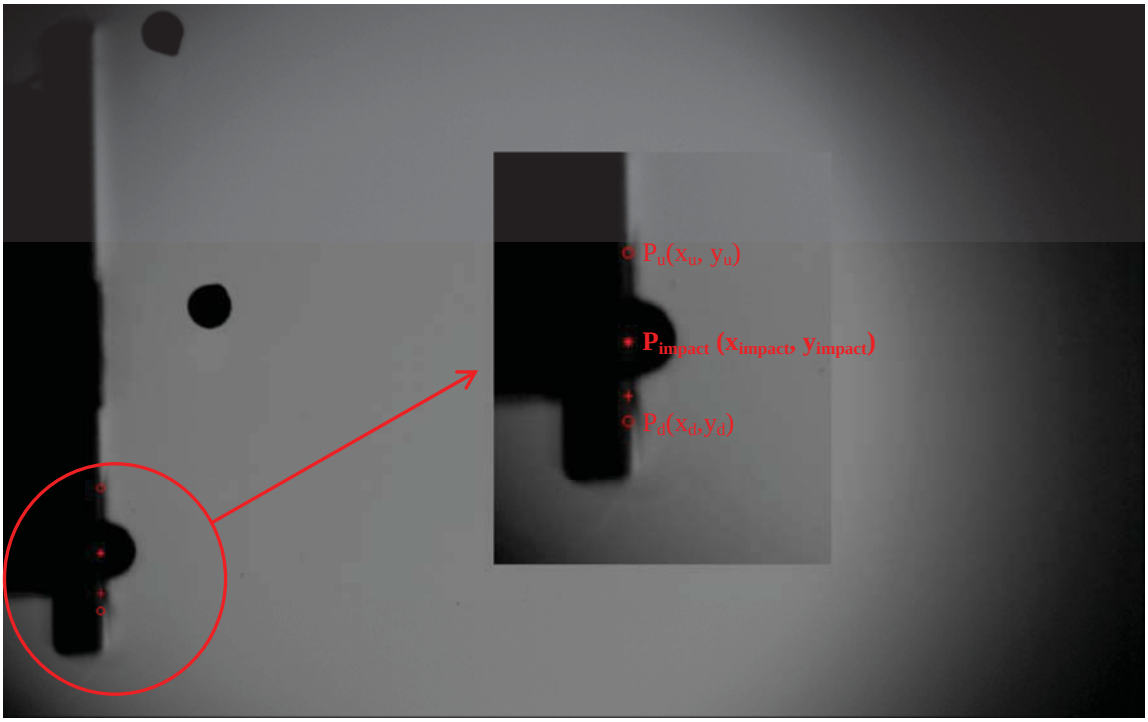

ximpact	yimpact	Cloud Velocity Down	Cloud Velocity Up	Wedge Velocity
Pixels	Pixels	m/sec	m/sec	m/sec
-430.0	617.9	-326.3	388.1	120.2

Figure 17. Run 96 071213. The ice particle is captured at the instant of impact. V_{wedge} = 120.2 m/sec; vertical velocity of ice particle $V_{particle}$ = 10.3 m/sec; wedge angle 0^o, ice particle diameter = 1.7 millimeters; camera frame rate = 6100 fps; resolution = 27.5 pixels/millimeter. The particle impact point $P(x_{impact}, y_{impact})$ and the upper and lower limits of the fragment cloud, $P(x_u, y_u)$ and $P(x_d, y_d)$, are labeled.